Magnesium-doped zinc oxide nanorod–nanotube semiconductor/p-silicon heterojunction diodes

Yasemin Caglar[1] · Kamuran Görgün[2] · Saliha Ilican[1] · Mujdat Caglar[1] ·
Fahrettin Yakuphanoğlu[3]

Abstract Nanostructured zinc oxide material is usable in electronic device applications such as light-emitting diodes, heterojunction diode, sensors, solar cell due to its interesting electrical conductivity and optical properties. Magnesium-doped zinc oxide nanorod (NR)–nanotube (NT) films were grown by microwave-assisted chemical bath deposition to fabricate ZnO-based heterojunction diode. It is found that ZnO hexagonal nanorods turn into hexagonal nanotubes when the Mg doping ratio is increased from 1 to 10 %. The values of the optical band gap for 1 % Mg-doped ZnO NR and 10 % Mg-doped ZnO NT films are found to be 3.14 and 3.22 eV, respectively. The n-ZnO:Mg/p-Si heterojunction diodes were fabricated. The diodes exhibited a rectification behavior with ideality factor higher than unity due to the presence of surface states in the junction and series resistance. The obtained results indicate that Mg doping improves the electrical and optical properties of ZnO.

1 Introduction

As one of the noticeable materials, nanostructured zinc oxide (ZnO) has been significantly investigated for its versatile physical and chemical properties. In the years

since 2000, ZnO has been explored in the fields of electronics and optoelectronics. Different morphologies of ZnO nanostructures, such as nanowire arrays [1, 2], nanorods [3], nanobelts [4] and nanotubes [5], have been deposited using physical and chemical methods. Tube-shaped nanocrystals having larger surface area have attracted much attention according to other crystal structures, and this feature increases its potential applications in areas such as photocatalysis [6], solar cells [7] and chemical sensors [8]. Compared to the deposition techniques used to obtain ZnO nanotubes, low-temperature solution growth process comes forward because of its simplicity and ease of fabrication.

Doping process has been used to control the properties of semiconductors in most electronic devices. In particular, for ZnO, Mg can be considered as an important dopant due to the similarity of ionic radii of Zn and Mg. The widening of optical band gap of ZnO with Mg doping makes ZnO an appealing material for possible applications in solid-state lighting and heterostructures, and also they have been extensively studied for light-emitting diode [9], solar cells [10], sensors [11], field-effect transistors [12]. There are various methods related to production of Mg-doped ZnO such as magnetron sputtering [13], pulsed laser deposition [14], spray pyrolysis [15], sol–gel [16, 17] and chemical bath deposition (CBD) [18, 19]. Naturally, CBD method has a great advantage due to low-cost film formation, homogeneous and high-quality films. CBD is a simple method, which basically provides a nucleation and crystal growth on substrate inside the solution, resulting in the formation of metal oxide films. This method has been commonly used in synthesis of nanostructure films. Compared with traditional water bath heating, the main advantage of microwave synthesis is to heat rapidly the whole volume of the solution uniformly by controlling the

✉ Mujdat Caglar
  mcaglar@anadolu.edu.tr

[1] Department of Physics, Faculty of Science, Anadolu University, 26470 Eskisehir, Turkey

[2] Department of Chemistry, Faculty of Arts and Science, Eskisehir Osmangazi University, 26480 Eskisehir, Turkey

[3] Department of Physics, Faculty of Science, Fırat University, Elazığ, Turkey

temperature precisely [20] and to require very short reaction times, resulting in less energy consumption. Besides, microwave irradiation, which causes the heat created inside the material, has been widely used as a heating method in chemistry and material synthesis. Shape- and size-selective ZnO nanostructures having nanorod and nanotubes shapes can be fabricated by a microwave-assisted chemical bath deposition (MW-CBD) method that their diameters can be systematically varied over hundreds of nanometers. In the available literature, there are no studies about Mg-doped ZnO film synthesized by MW-CBD method, but there exist few studies made using CBD method. Among those reported, Chandramohan et al. [19] deposited the undoped and Mg-doped ZnO using a modified two-step chemical bath deposition technique and reported a shifting toward to lower wavelengths in the absorption edge with respect to Mg incorporation. They also reported an increase in grain size and an agglomeration with less voids on surface of the film. Polat et al. [21] deposited 2, 4 and 6 % Mg-doped ZnO films by CBD method onto ZnO-seeded FTO substrates. In their report, it is emphasized that optical band gap of ZnO nanorods having hexagonal crystal structure increased to 4 at% Mg doping and then decreased, and also as a result of solar cell measurements, an enhancement in efficiency was found with increasing Mg doping to 4 at%. Vijayaprasath et al. [18] used the CBD method to prepare Mg-doped ZnO film on the glass substrate. They reported a blue shift in the optical band gap with respect to Mg doping and that the flower-shaped structure of pure ZnO converted into spherical.

There exist so many studies on Mg-doped ZnO having nanorod structure obtained by CBD, but among these works it has so far not encountered with nanotubes structures. Most of previous studies have focused on nanotube films and powder forms of undoped ZnO. For example, Roza et al. [22] synthesized ZnO nanotubes onto FTO substrate by hydrothermal method. In this work, it was reported that hexamethylenetetramine (HMT) and precursor concentration could play an important role in the modification of the shape and density of ZnO nanostructure. Likewise, Wang et al. [23] deposited c axis-oriented ZnO nanorod (NR) arrays by CBD and reported that the variation of precursor concentration helps to control NRs' mean diameter and the increase in the growing time leads to changes in ZnO nanotube structure.

In the scope of the application, there are some works about heterojunction diode based on Mg-doped ZnO deposited by various method. Some scientists such as Singh et al. [24] and Huang et al. [25] were devoted to the study of Mg-doped ZnO-based Schottky diode as heterojunction one is very limited. Soylu and Savas [26] investigated the electrical parameters of Mg-doped ZnO-based heterojunction diodes deposited by sol–gel spin coating

method and reported that being controlled these parameters by doping amount. Tsuboi et al. [27] exhibited rectifying properties of p-Si/n-$Mg_{0.05}Zn_{0.95}O$ heterojunction fabricated using a remote plasma-enhanced metalorganic chemical vapor deposition method.

In this work, Mg-doped ZnO films having nanotube-shaped surface morphology deposited by MW-CBD have been firstly reported and there is no significant study about its heterojunction diode application. Hence, the aim of this work is to investigate the effects of Mg concentration on the microstructure and optical properties and to make the electrical characterization of p-Si/n-ZnO:Mg heterojunction by using I–V and C–V measurements.

2 Experimental details

2.1 Chemicals

Zinc nitrate hexahydrate [$Zn(NO_3)_2.6H_2O$, ZnNt], hexamethylenetetramine ($C_6H_{12}N_4$, HMTA) and magnesium nitrate [$Mg(NO_3)_2$, MgNt] were used to prepare the solutions. All chemicals were purchased from Sigma-Aldrich. The solutions were prepared with deionized (DI) water purified with a Merck Millipore Direct Q3 (18.2 MΩ,). p-Si (Boron doped, <100>, 600–650 μm, 1–10 Ω-cm) substrates were purchased from Montco Silicon Technologies Inc.

2.2 Deposition of Mg-doped ZnO NR–NT films

Mg-doped ZnO NR–NT films were deposited on p-Si substrates using a MW-CBD method without any template. Firstly, p-Si substrates were cleaned ultrasonically in deionized water and acetone for 10 min and then were dried with N_2 flow. Then, the substrates were cleaned in argon plasma cleaner (Harrick) for 10 min. Secondly, the solutions were prepared. For this, ZnNt and MgNt were used as precursor materials and doping source materials, respectively. To stirred ZnO precursor, solution with the concentration of 0.1 M of ZnNt was made by dissolving 100 ml of deionized water. The next process is to add the certain amount of HMTA catalyst to accelerate the reaction, and supply of OH^- as capping agent promotes anisotropic growth. Various amount of doping precursor MgNt corresponding to 0.0297 and 0.297 g (1 and 10 %, respectively) was added separately into the aqueous ZnNt + HMTA solutions. The mixture was stirred using a magnetic stirrer for 20 min in room temperature. The p-Si substrate was inserted in a beaker containing this solution. Finally, the first solution immersing the Si substrate was transferred into a CEM Mars 6 model microwave oven and irradiated at 600 W for 10 min. After MW treatment, the
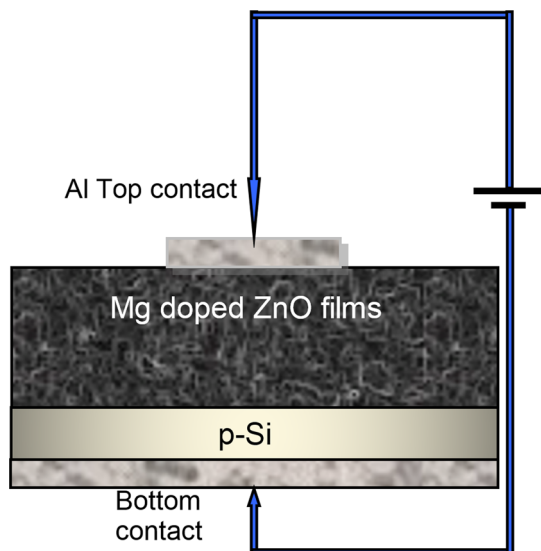
Fig. 1 Schematic diagram of n-ZnO/p-Si heterojunction structure

film was removed from the solution and rinsed with deionized water and dried under N_2 flow and then the film dried at 60 °C for 1 h. The same procedure was made for other film.

2.3 Fabrication of n-ZnO/p-Si heterojunction diodes

In the heterojunction fabrication process, firstly, for top ohmic contact, the highly pure aluminum was thermally evaporated as 100 nm thickness in the pressure of 4.5×10^{-5} Torr. The contacts formed in the form of circular dots have 0.5 mm in diameter. For back contact, silver paint was used. The schematic structure of the heterojunction diode is shown in Fig. 1.
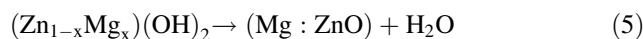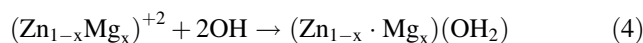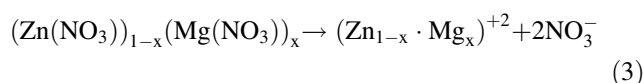
2.4 Characterization of Mg-doped ZnO NR–NT films

Bruker D2 Phaser X-ray powder diffractometer equipped with CuK_α radiation ($\lambda = 1.5418$ Å) was used to check the crystalline phase and crystallite orientation of Mg-doped ZnO NR–NT films. For surface morphology studies, Zeiss Ultraplus scanning electron microscope (SEM) was used. The diffuse reflectance measurements of the films were taken by Shimadzu 2450 spectrophotometer, including an integrating sphere attachment with using barium sulfonate ($BaSO_4$) as reference. The current–voltage (*I–V*) and capacitance–voltage (*C–V*) measurements were taken inside Signatone probe station using a Keithley 4200 semiconductor characterization system.

3 Results and discussion

3.1 Reaction mechanism of Mg-doped ZnO

The main reaction mechanism has been elucidated through the identification of reaction products and intermediates. This mechanism most often referenced in the literature for ZnO nanorod deposition from ZnNt and HMTA. Understanding the growth mechanism of the Mg-doped ZnO NR–NT films, the process based on decomposition or hydrolysis of zinc and magnesium salts can be proposed for the formation of ZnO in aqueous solution. During the thermal decomposition in aqueous solution in the form of zinc magnesium hydroxide precursors, the Zn^{2+} and Mg^{2+} derive from ZnNt and MgNt, respectively, and also OH^- releases from HMTA. As a result, a nucleation of Mg-doped ZnO NR–NT starts to grow on the substrate. The main chemical reaction process can be described as

$$C_6H_{12}N_4 + 6H_2O \rightarrow 6HCHO + 4NH_3 \tag{1}$$

$$NH_3 + H_2O \rightarrow NH_4^+ + OH^- \tag{2}$$

$$(Zn(NO_3))_{1-x}(Mg(NO_3))_x \rightarrow (Zn_{1-x} \cdot Mg_x)^{+2} + 2NO_3^- \tag{3}$$

$$(Zn_{1-x}Mg_x)^{+2} + 2OH \rightarrow (Zn_{1-x} \cdot Mg_x)(OH_2) \tag{4}$$

$$(Zn_{1-x}Mg_x)(OH)_2 \rightarrow (Mg : ZnO) + H_2O \tag{5}$$

Here, HMTA decomposes to form formaldehyde and ammonia (Eq. 1). Ammonia reacts with water to produce OH^- (Eq. 2). The reaction between ZnNt, various amount of doping precursor MgNt and OH^- as a result forms Mg-doped ZnO by MW irradiation (Eqs. 3, 4, 5). With this reaction process, if the p-Si substrate is immersed in the solution, the attractive forces occurring between ions in the solution and the substrate surface cause an adsorption of zinc complex ions on the substrate. Wherein, the mentioned forces may be cohesive, or Van der Waals, or chemical attractive.

3.2 Morphological analysis of the ZnO NR and ZnO NT films

Field emission scanning electron microscopy (FESEM) has been used to investigate the surface morphology of the films. FESEM images in Fig. 2 show the effect of incorporation of Mg in the ZnO lattice on the surface morphology. Hexagonal rods cover all the surfaces as seen from the top views at different magnifications. It is found that ZnO hexagonal nanorods turn into hexagonal nanotubes when the Mg doping ratio is increased from 1 to 10 %. While in Fig. 2a, b ZnO hexagonal rods are verti-
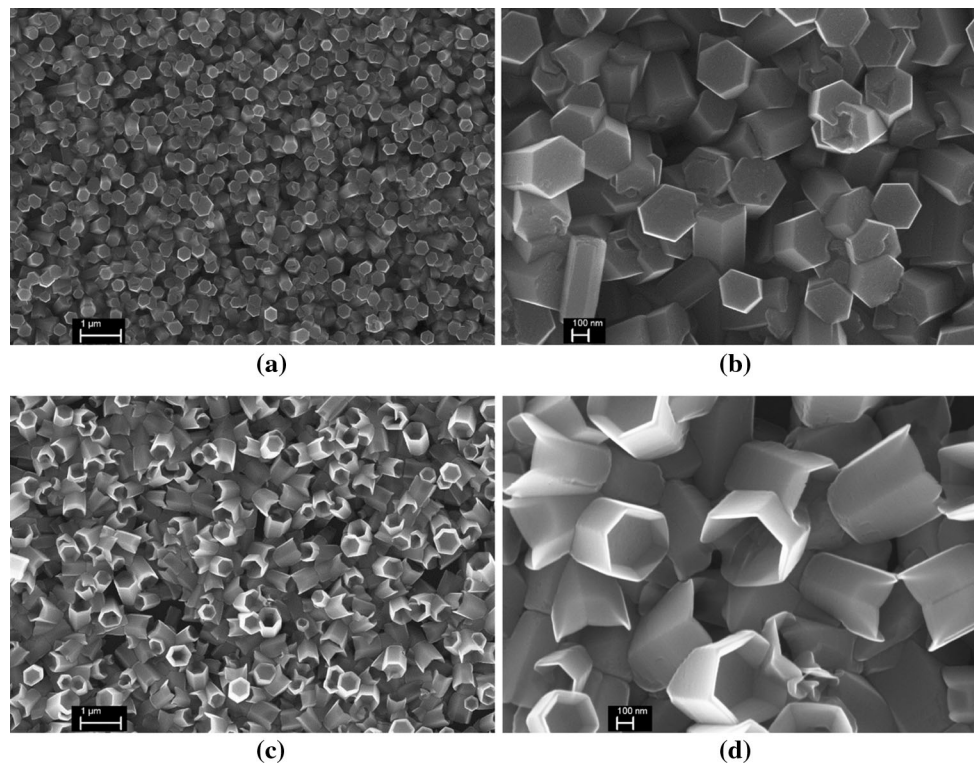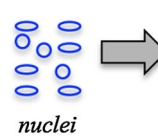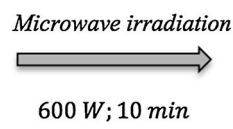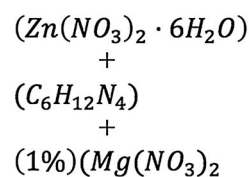
Fig. 2 FESEM images of 1 % Mg-doped ZnO-NR and 10 % Mg-doped ZnO-NT films at 25 k (**a**, **c**) and 100 k (**b**, **d**) magnifications

cally well aligned on the surface, this alignment is slightly lost in Fig. 2c, d, resulting in a decrease in density with contributions of hollow cores inside hexagonal nanorods. Thus, it is clearly seen the morphological transformation of nanorods to nanotubes with increase in doping. It is also observed an increase in rod diameter with increasing Mg doping. One and 10 % Mg-doped ZnO films are named ZnO NR and ZnO NT, respectively.
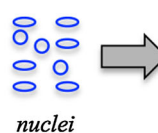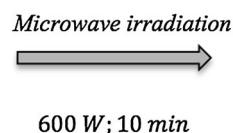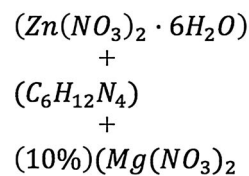
3.3 Growth mechanism of the ZnO NR and ZnO NT

The mechanism of interaction of HMTA with ZnNt, and MgNt in microwave oven cell is shown in Fig. 3. The growth mechanism of ZnO nanorods and nanotubes is shown in Fig. 2a, b. The structure of ZnO was doping controlled for 1 % Mg doping and 10 % Mg doping. For 1 % Mg doping, ZnO nanocrystals are grown in nanorods
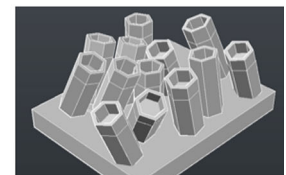
Fig. 3 Scheme of growth mechanism for the ZnO NR (**a**) and ZnO NT (**b**)
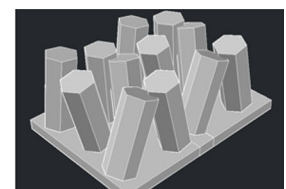
shape. After 10 % Mg doping, ZnO is grown drastically as nanotube shape ZnO nanocrystals. Addition of Mg atoms changes the growth rate preference along different crystal axes of ZnO. Therefore, ZnO is transformed from the nanorods to nanotubes in crystal morphology. This transformation with Mg doping suggests that the increase in Mg content is an important factor that causes a change from nanorods to nanotubes in the ZnO structural morphology.

3.4 Structural analysis of the ZnO NR and ZnO NT films

The crystal structure is defined simply as the ordered arrangement of atoms or molecules in a crystalline material, and also it plays an important role in determining the physical properties of any materials. Herewith, to know the effect of Mg doping on the crystal structure of ZnO, X-ray powder diffraction (XRD) analysis was carried out and as a result of the measurements a significant effect was observed as shown in Fig. 4. Figure 4 shows the XRD patterns, presenting the formation of the hexagonal wurtzite ZnO crystal structure (JCPDS reference 36-1451) having the polycrystalline nature. Diffraction peaks belong to (100), (002), (101), (102) and (110) planes are also shown in Fig. 4, and no other impurity phase such as Mg,
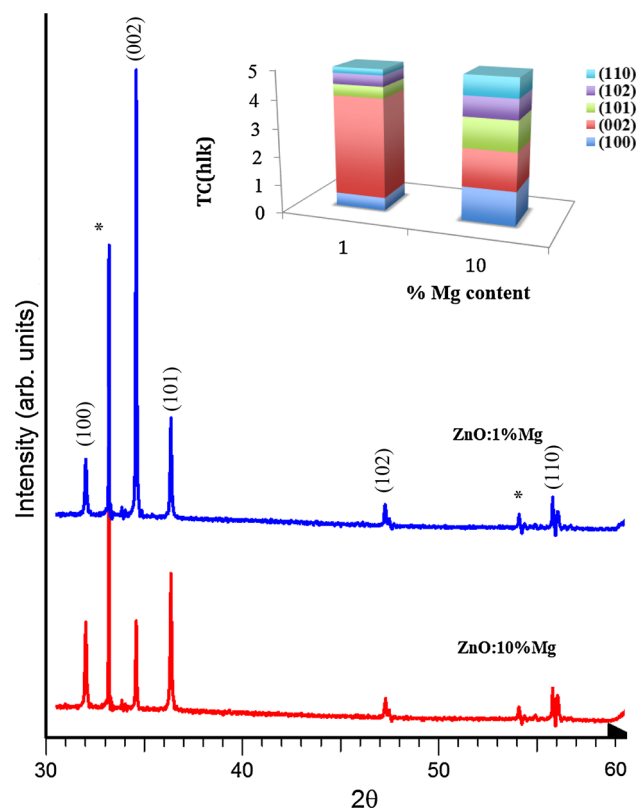
MgO is identified, which also means that Mg ion successfully occupies the lattice site rather than interstitial ones. Also peaks at 33.1° and 54.6° belong to Si substrate. While, in the first pattern, (002) reflection peak intensity is quite high, the intensities of the other peaks have changed significantly with incorporation of Mg into the ZnO lattice at a ratio of 10 %. This situation can be explained by the reduction in the concentration of the zinc interstitials for charge compensation, which resulted in suppressed ZnO grain growth and deteriorated crystallinity [28]

Compared with the relative intensities of the peaks obtained form XRD patterns with their standard values, the information about preferential growth can be obtained. The texture coefficient TC(hkl) describes the texture of the particular plane, and deviation from unity of this expression indicates the preferential growth orientation. The TC(hkl) values for five different orientations of the samples were calculated using the following relation [29] and given in inset of Fig. 3,

$$TC(hkl) = \frac{I(hkl)/I_o(hkl)}{N^{-1}\sum\limits_{n} I(hkl)/I_o(hkl)} \tag{6}$$

where $I(hkl)$ is the measured relative intensity of a plane (hkl), $I_o(hkl)$ is the standard intensity of the plane (hkl) taken from the JCPDS data, N is the number of reflection, and n is the number of diffraction peaks. Random orientation of all the crystallites means that texture coefficient is equal to 1. Actually, an increase in the amount of deviation from unity in the texture coefficient indicates a higher degree of preferred orientation along a particular plane as compared to the bulk. The values of texture coefficients calculated from the diffraction peaks are presented in inset of Fig. 4. Comparison of the texture coefficients of different planes reveals that the ZnO NR film is highly textured along the (002) plane having the highest packing fraction of planar density in the wurtzite structure. Decrease in texture coefficient of (002) plane with increasing Mg content is a sign of deterioration of the crystal structure.

3.5 Optical band gap of the ZnO NR and ZnO NT films

A transmittance spectrum is the most appropriate and simple method used to determine the optical band gap energy, but the optical transmission measurements may not be possible in case of opaque or powder sample. Therefore, for studying the optical band gap energy of such samples, the reflectance (R) spectrum can also be used. The determination of the band gap via the diffuse reflectance measurements of an opaque substrate is a standard technique. To determine the optical band gap of ZnO NR and ZnO NT films deposited on the p-Si wafer, the diffuse reflectance
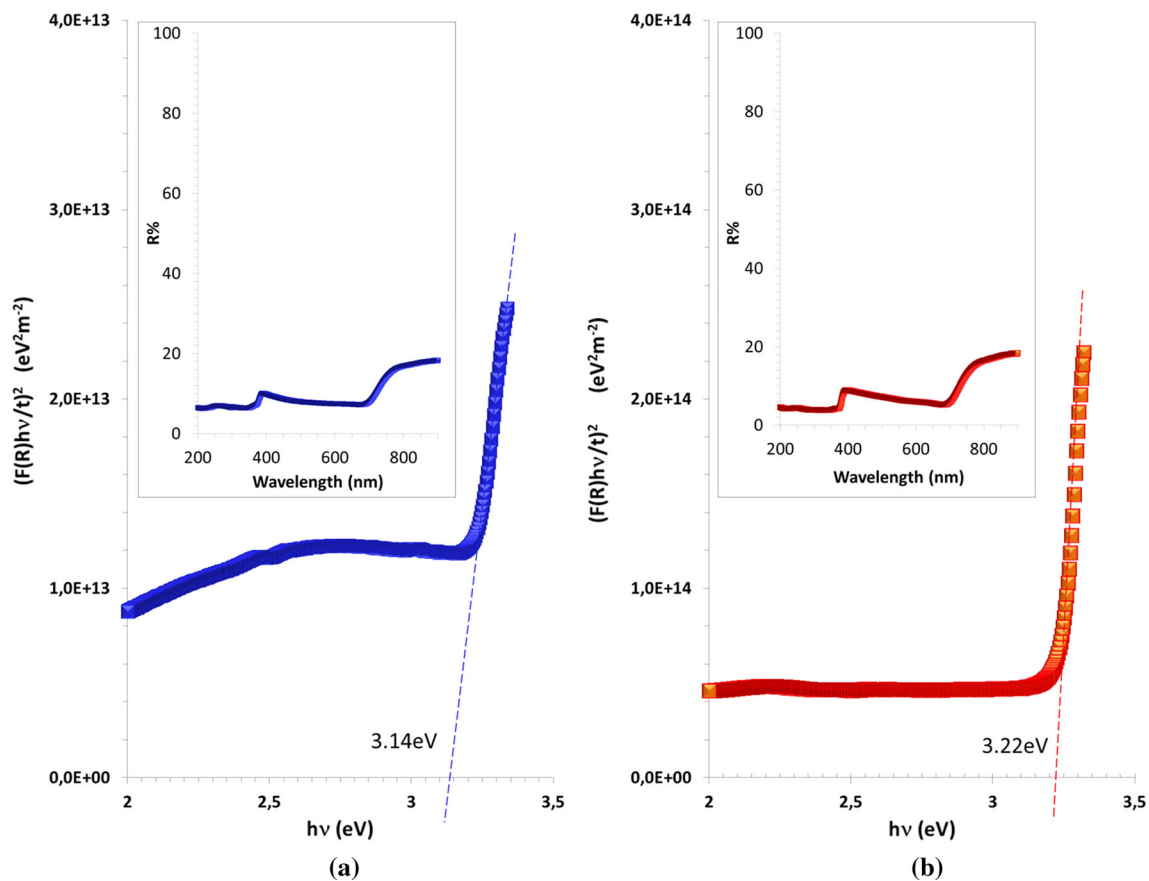

Fig. 4 XRD spectra of ZnO-NR and ZnO-NT films and the variation of TC(hkl) values with Mg content inset of figure

Fig. 5 **a** Kubelka–Munk graph and reflectance spectra of ZnO-NR film the inset of figure **b** Kubelka–Munk graph and reflectance spectra of ZnO-NT film the *inset* of figure

spectra have been used. As shown in inset of Fig. 5a, b, the average reflectance is found to be 9.37 and 8.15 % (at 400–800 nm) for the ZnO NR and ZnO NT films, respectively. The reflectance values converted to absorbance by application of the Kubelka–Munk function were used to determine the value of optical band gap of the films. In general, the Kubelka–Munk theory, by analyzing the obtained diffuse reflectance spectra, is used to determine the concentration of an absorbing species [30]:

$$F(R) = \frac{(1-R)^2}{2R} \qquad (7)$$

where $F(R)$ is Kubelka–Munk function corresponding to the absorbance and converting it to the linear absorption coefficient is expressed by the following relation

$$a = \frac{F(R)}{t} = \frac{\text{Absorbance}}{t} \qquad (8)$$

where t is the thickness of the films.

Equation (7) can be rewritten as

$$\left(\frac{F(R)h\nu}{t}\right) = A\left(h\nu - E_g\right)^n \qquad (9)$$

The optical band gap values for ZnO NR and ZnO NT films have been obtained by extrapolating the linear portion of the plots of $[F(R)h\nu/t]^2$ versus the photon energy to $h\nu = 0$ as shown in Fig. 5a, b. The values of the optical band gap for ZnO NR and ZnO NT films are found to be 3.14 and 3.22 eV, respectively. Although the obtained results are consistent with many of the previous studies [31–34], they are lower than the known band gap energy of bulk ZnO (3.37 eV). This decrease may be attributed to some defects which exist within the ZnO lattice such as ionized Mg impurity atoms and native defects [35]. The observed increase in optical band gap with high Mg doping can be explained by the Burstein–Moss effect, and different research groups reported the same expansion in the band gap due to the increase in Mg content [36, 37].

3.6 Current–voltage characteristics of the n-ZnO NR/p-Si and n-ZnO NT/p-Si heterojunction diodes

The electrical characterizations of the fabricated nanostructure n-ZnO/p-Si heterojunction diodes were carried out
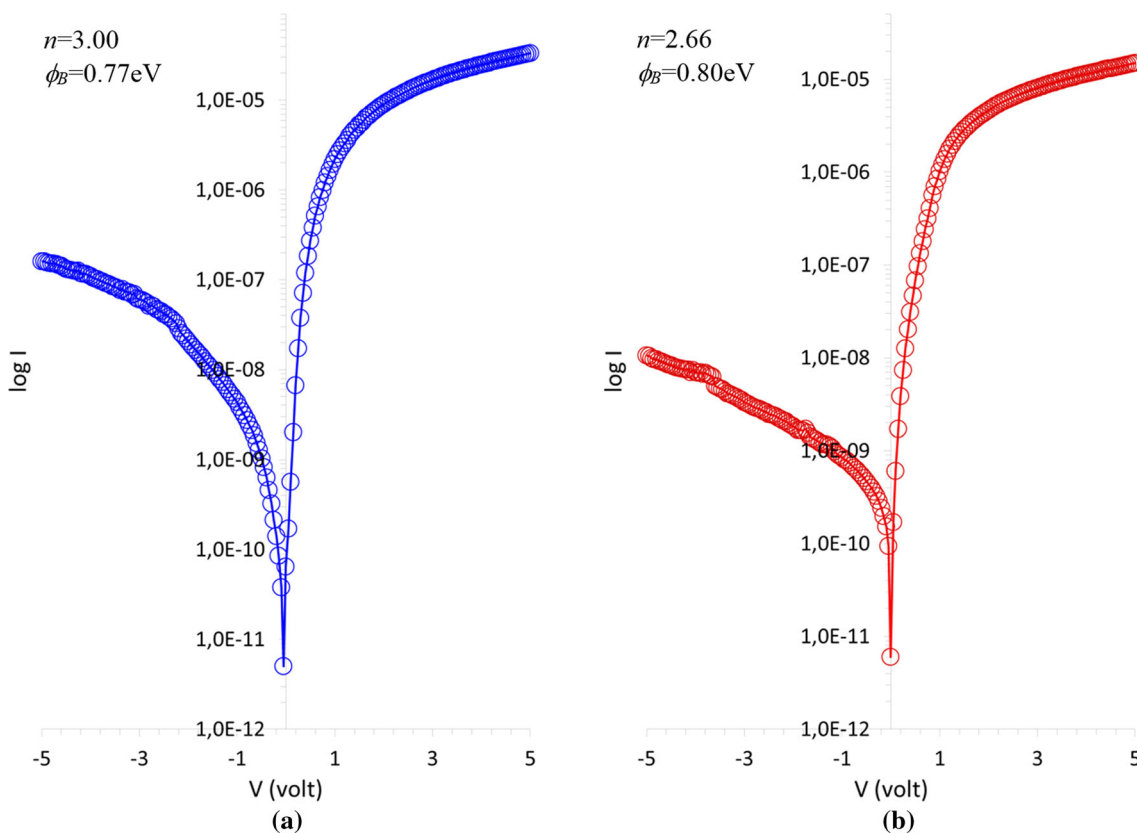
Fig. 6 Forward and reverse log *I–V* plots of n-ZnO-NR/p-Si (**a**) and n-ZnO-NT/p-Si (**b**), respectively

at room temperature in air under dark conditions. Figure 5 shows the experimental semilog *I–V* characteristics of n-ZnO NR/p-Si and n-ZnO NT/p-Si heterojunction diodes having a rectification property. The following relation [38] can be used to determine the diode parameters using the *I–V* characteristic.

$$I = AA^*T^2 \exp\left(-\frac{q\emptyset_b}{kT}\right)\left[\exp\left(\frac{qV}{nkT}\right) - 1\right] \quad (10)$$

where *V* is the applied bias voltage, *q* is the charge, *n* is the ideality factor, *k* is the Boltzmann constant, and *T* is the absolute temperature in Kelvin. The reverse saturation current I_s which is determined from the straight-line intercept of ln *I–V* plot at zero-bias is given by,

$$I_s = AA^*T^2 \exp\left(-\frac{q\emptyset_b}{kT}\right) \quad (11)$$

where *A* is the rectifier contact area, A^* is the effective Richardson constant (32 A/cm^2 K^2 for p-type Si), and $\emptyset_b$ is the barrier height at zero-bias easily obtained from Eq. (11). By using Eq. 11, the ideality factor *n* can be calculated from the slope of the linear region of the forward bias ln *I–V* plot and can be expressed as,

$$n = \frac{q}{kT}\left(\frac{\mathrm{d}V}{\mathrm{d}(\ln I)}\right) \quad (12)$$

Also, if Eq. 12 is reorganized according to the barrier height, it can be written by

$$\phi_b = \frac{kT}{q}\ln\left(\frac{AA^*T^2}{I_s}\right) \quad (13)$$

The calculated values of *n* and ϕ_b for n-ZnO NR/p-Si and n-ZnO NT/p-Si heterojunction diodes are shown in Fig. 6. Both ideality factors calculated as 3.00 and 2.66 from the slope of the linear region of Fig. 6 for two different Mg doping are larger than unity. Actually that being larger than unity of these values may be acceptable for a heterojunction and generally the presence of surface states in the junction is the reason of this deviation from ideal behavior. Also, the possible oxide layer on the p-Si and the series resistance effect significantly affect the ideality factor of the diode. For obtaining barrier height, Eq. (7) was used and ϕ_b values were calculated as 0.77 and 0.80 eV. Considering that the difference between the work functions of Si and ZnO is 0.72 eV, the calculated values in this work are within acceptable limits. When both *n* and ϕ_b values
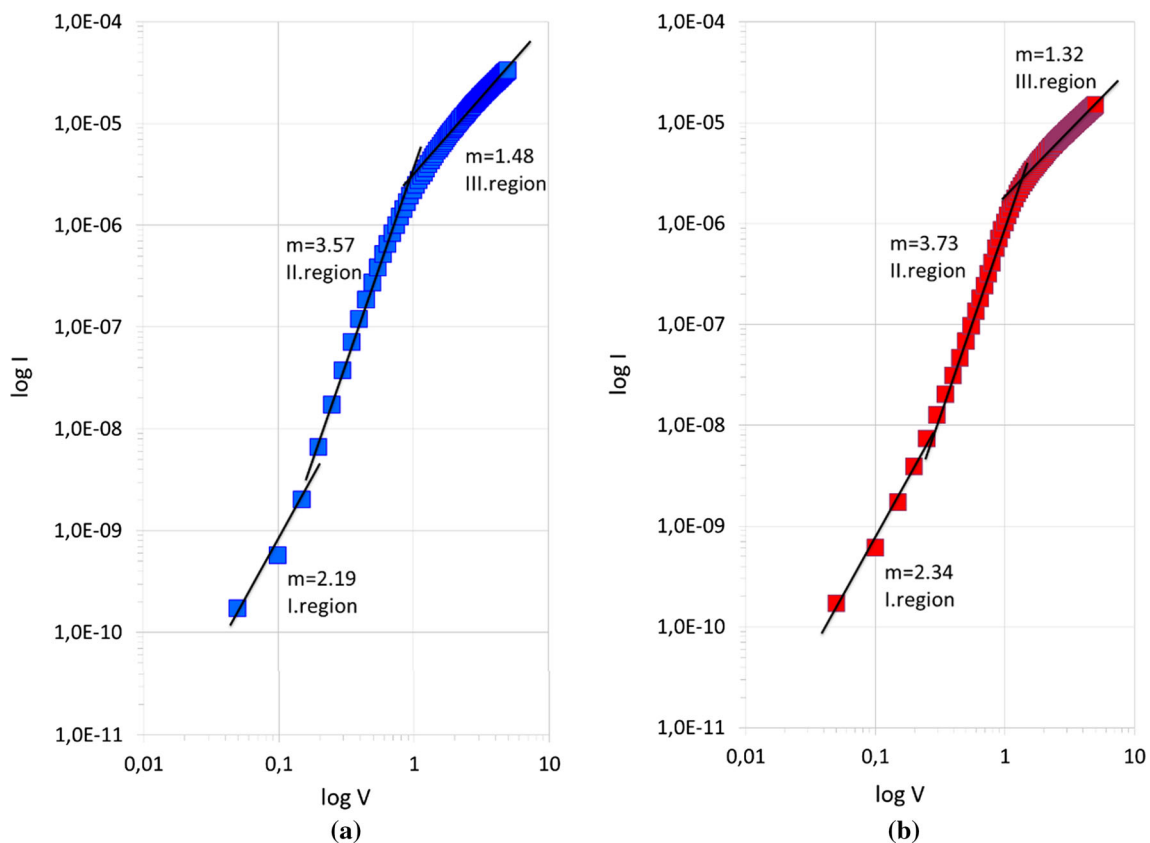
Fig. 7 log I–log V plot of n-ZnO-NR/p-Si (**a**) and n-ZnO-NT/p-Si (**b**), respectively

are compared with the literature, it can be seen that these parameters are better than the values obtained in earlier published works which is related to ZnO-based heterojunction [39–42]. As above mentioned that the ideality factor is higher than unity probably originates from the presence of an interfacial layer and traps at the interface of heterojunction. The curves of log I versus log V (see Fig. 7a, b) were plotted to evaluate the conduction mechanism controlling the heterojunction diode behavior. Then, these plots were analyzed according to power law, $I\alpha V^m$ relation. Both Fig. 6a, b contain three different linear regions, indicating different conduction mechanisms, and the slopes of these regions were calculated to detect m values. These different slopes can exhibit the charge transport mechanisms being changed by the presence of traps at the interface. For both heterojunctions, all the slopes belong to three regions are approximately same and in region I ($0.05 \leq V \leq 0.2$), the calculated slopes (m) are 2.19 and 2.34, respectively. These slopes suggest that the conduction mechanism in this voltage region is controlled by the space charge-limited current (SCLC) mechanism. Because the expected value of m is 2 in the region-dominated SCLC mechanism [43, 44]. The slopes of 3.57 and

3.73 observed in region II ($0.2 \leq V \leq 1$) mean that the conduction mechanism is controlled by trap charge-limited current (TCLC). In this mechanism, the energy distribution of trap levels within the forbidden band causes the slope to be greater than 2 [45]. Also, at the voltages ($1 \leq V \leq 7$) (region III), the value of m was determined as 1.48 and 1.32. These slopes values mean that the current approaches the space-limited region due to the filled all traps [44, 46].

Cheung's method can be used to analyze the series resistance effect playing an important role on the diode parameters [47]. In this method, the forward bias I–V characteristics of a diode deviating from linearity due to series resistance effect are expressed as:

$$I = I_s \exp\left[\frac{q(V - \mathrm{IR}_s)}{nkT}\right] \tag{14}$$

where the IR_s is the voltage drop across the series resistance of nanorod heterojunction diode. The values of series resistance, ideality factor and barrier height are calculated by the following equation:

$$\frac{\mathrm{d}V}{\mathrm{d}(\ln I)} = \mathrm{IR}_s + n\left(\frac{kT}{q}\right) \tag{15}$$

Fig. 8 dV/d ln(I)–I and H(I)–I plots of n-ZnO-NR/p-Si (a) and n-ZnO-NT/p-Si (b), respectively

(a)

(b)
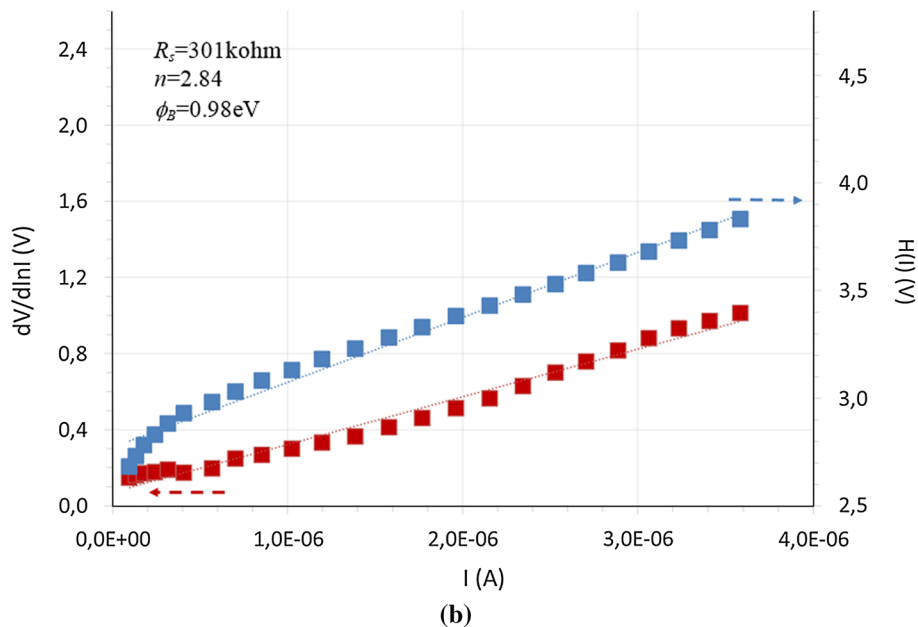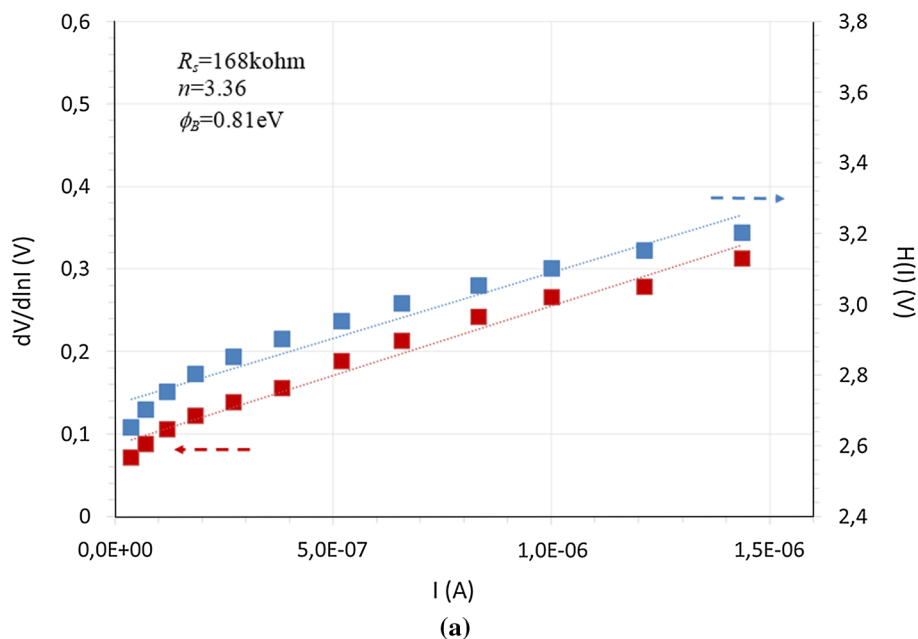
$$H(I) = V - n\left(\frac{kT}{q}\right) \ln\left(\frac{I}{AA^*T^2}\right) \quad (16)$$

where

$$H(I) = IR_s + n\emptyset_b \quad (17)$$

The slope and the y axis intercept of the dV/d ln(I) versus I plot which is shown in Fig. 8 are used to calculate R_s and n. These values are obtained as 168 kΩ and 3.36 for n-ZnO-NR/p-Si diode, 301 kΩ and 2.84 for n-ZnO-NT/p-Si diode, respectively. The intercept of H(I) versus I plot shown in Fig. 8 was used to determine ϕ_b values and

calculated as 0.81 and 0.98 eV, respectively. This n value is slightly different obtaining from the forward bias In I–V plot, resulting from the presence of series resistance and interface states [48].

In order to identify the effect of series resistance on I–V characteristics, alternative method is Norde method. The following function has been defined in the modified Norde's method [49]:

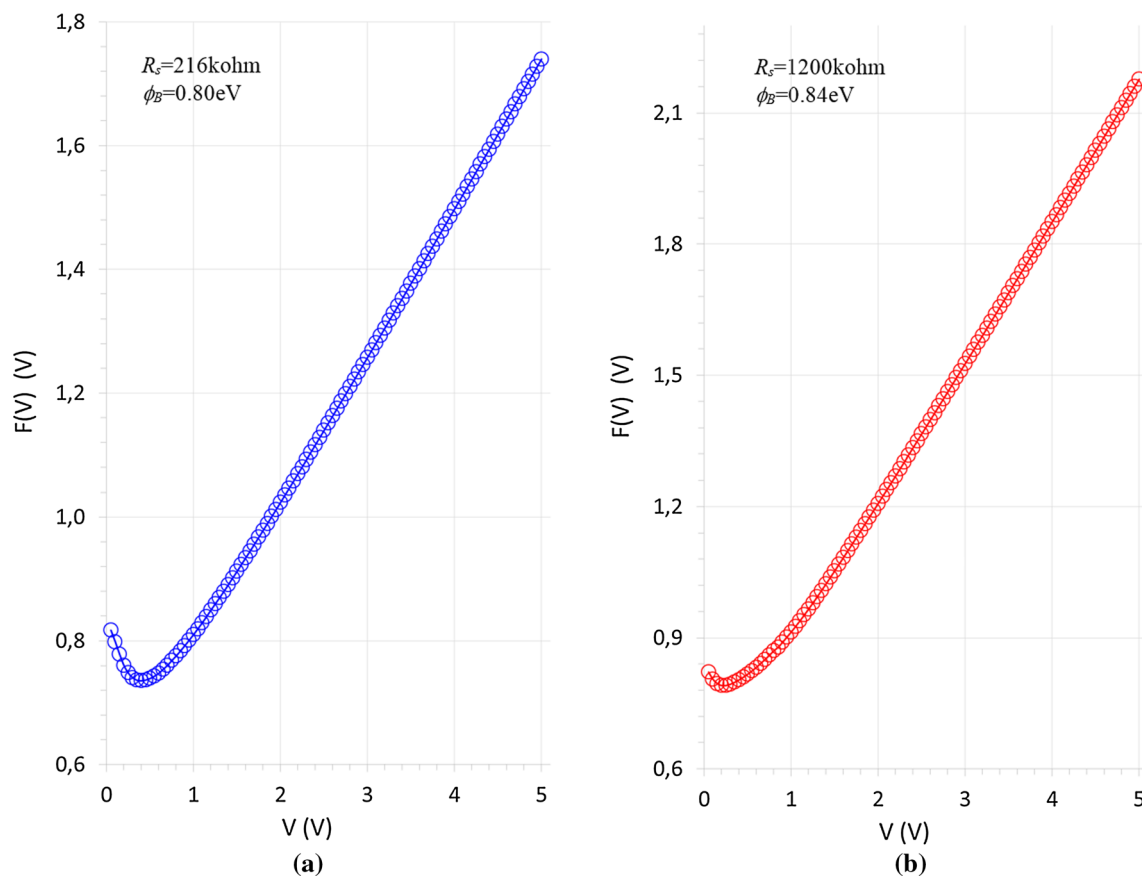$$F(V) = \frac{V_0}{\gamma} - \frac{kT}{q} \ln\left(\frac{I(V)}{A^*AT^2}\right) \quad (18)$$

Fig. 9 $F(V)$–V plots of n-ZnO-NR/p-Si (**a**) and n-ZnO-NT/p-Si (**b**), respectively

where γ is the integer (dimensionless) greater than n and $I(V)$ is the current obtained from the I–V characteristic. Figure 9 shows the plot of $F(V)$ versus voltage. The $\varnothing_b$ and the R_s for the nanorod heterojunction diodes are calculated by the following equation:

$$\phi_b = F(V_0) + \frac{V_0}{\gamma} - \frac{kT}{q} \tag{19}$$

$$R_s = \frac{kT(\gamma - n)}{qI_0} \tag{20}$$

where $F(V_0)$ is the minimum point of $F(V)$. By using the Norde Method, the barrier height and series resistance values of n-ZnO-NR/p-Si and n-ZnO-NT/p-Si were calculated to be 0.80 and 0.84 eV and 216 and 1200 kΩ, respectively. The reason of difference between series resistance values obtained from both Cheung and Norde's methods may be due to the fact that Cheung's model is applicable in high-voltage region, while Norde's model is applied to the full-voltage range [50]. We analyzed the effects of high electric fields on the I–V characteristics of the diodes. It is seen that I–V characteristics of the diodes are affected from low and high electric fields. Thus, it is

evaluated that the Norde's method is suitable for the system.

3.7 Capacitance–voltage of n-ZnO-NR/p-Si and n-ZnO-NT/p-Si heterojunction diode

In the investigation of capacitance–voltage (C–V) characteristics of n-ZnO-NR/p-Si and n-ZnO-NT/p-Si heterojunctions, C–V and $1/C^2$–V plots, which were taken at 10 kHz, were used are and shown in Fig. 10a, b. As shown in these figures, the capacitance value increases with the applied bias voltage and then reaches a constant value. The saturation region corresponds to oxide capacitance, C_{ox}, between ZnO and p-Silicon. The C_{ox} value is increased with Mg doping. A linear behavior of C–V curves was observed from 0.5 to 2 V due to the linear change in the depletion region of the diodes. The following relation can be used to analyze the C–V characteristics of the obtained heterojunction diodes [38]

$$\frac{1}{C^2} = \frac{2(V_{bi} + V)}{A^2 \varepsilon_s q N_a} \tag{21}$$

where V_{bi} is the built-in potential, ε_s is the dielectric constant of semiconductor ($\varepsilon_s = 11.8$), and N_a is the acceptor

Fig. 10 C–V and C^{-2}–V plots of n-ZnO-NR/p-Si (**a**) and n-ZnO-NT/p-Si (**b**) for 10 kHz, respectively
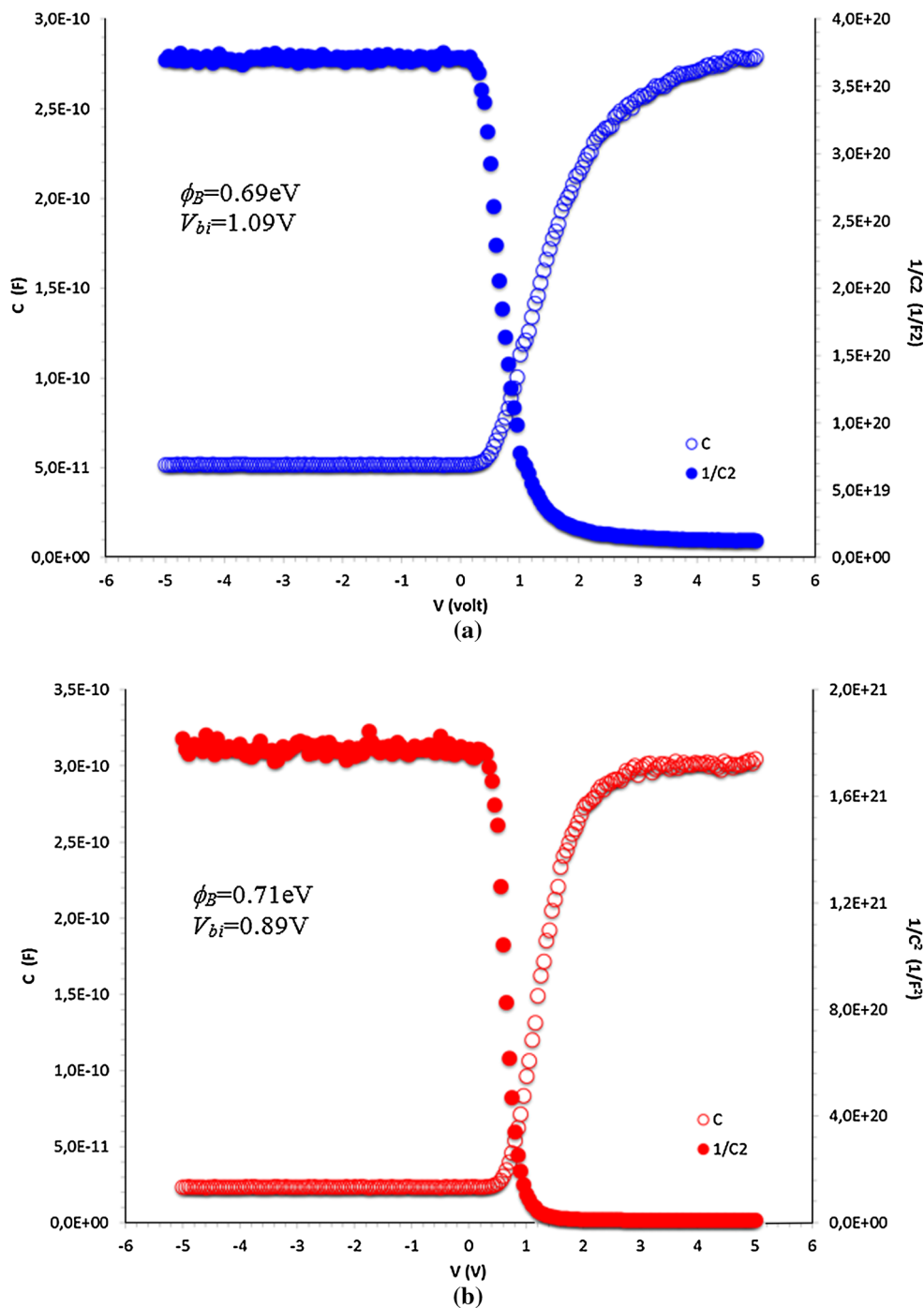
concentration. For the determination of barrier height of the diode from the C–V measurements, the following relation is used,

$$\phi_{b(C-V)} = V_{bi}/n + \frac{kT}{q}\ln\left(\frac{N_v}{N_a}\right) \qquad (22)$$

where N_v is density of states in the valence band ($N_v = 1.82 \times 10^{19}$ cm^{-3}). To calculate the barrier height values, the V_{bi} and N_a values obtained from C^{-2}–V plot were used. The obtained values for V_{bi} and ϕ_b are shown in Fig. 10. The ϕ_b values obtained from C–V are smaller than n values obtained from I–V, but it is closer to the difference between the work functions of Si and ZnO. This difference between barrier heights calculated with two different methods may result from the inhomogeneities such as non-uniformity of the interfacial layer thickness and distributions of the interfacial charges [38, 51].

4 Conclusions

Magnesium-doped zinc oxide nanorod–nanotube films were synthesized by microwave-assisted chemical bath deposition. SEM results indicate that Mg-doped ZnO is formed from the hexagonal nanorods. The optical band gap values of Mg-doped ZnO films are controlled from 3.14 to 3.22 eV with Mg doping. The rectifying properties of the diodes are changed with Mg incorporation. The diodes exhibited a nonlinear $I–V$ behavior with the calculated electronic parameters.

References

1. Z. Zhang, Y. Lv, J. Yan, D. Hui, J. Yun, C. Zhai, W. Zhao, J. Alloys Compd. **650**, 374 (2015)
2. C.-H. Kwak, H.-S. Woo, F. Abdel-Hady, A.A. Wazzan, J.-H. Lee, Sens. Actuators B Chem. **223**, 527 (2016)
3. B. Santoshkumar, S. Kalyanaraman, R. Vettumperumal, R. Thangavel, I.V. Kityk, S. Velumani, J. Alloys Compd. **658**, 435 (2016)
4. X. Qu, S. Lü, J. Wang, Z. Li, H. Xue, Mater. Sci. Semicond. Process. **15**, 244 (2012)
5. B. Huang, C. Zhao, M. Zhang, Z. Zhang, E. Xie, J. Zhou, W. Han, Appl. Surf. Sci. **349**, 615 (2015)
6. X. Dong, P. Yang, Y. Liu, C. Jia, D. Wang, J. Wang, L. Chen, Q. Che, Ceram. Int. **42**, 518 (2016)
7. L. Song, P. Du, J. Xiong, F. Ko, C. Cui, Electrochim. Acta **163**, 330 (2015)
8. C. Li, G. Shi, J. Photochem. Photobiol. C Photochem. Rev. **19**, 20 (2014)
9. H.-H. Huang, S.-Y. Chu, P.-C. Kao, Y.-C. Chen, Thin Solid Films **516**, 5664 (2008)
10. C. Tian, X. Chen, J. Liu, D. Zhang, C. Wei, Y. Zhao, X. Zhang, Appl. Surf. Sci. **314**, 786 (2014)
11. Y. Liu, T. Hang, Y. Xie, Z. Bao, J. Song, H. Zhang, E. Xie, Sens. Actuators B Chem. **160**, 266 (2011)
12. C.-Y. Tsay, H.-C. Cheng, M.-C. Wang, P.-Y. Lee, C.-F. Chen, C.-K. Lin, Surf. Coat. Technol. **202**, 1323 (2007)
13. S.-H. Jeong, J.-H. Park, B.-T. Lee, J. Alloys Compd. **617**, 180 (2014)
14. J.J. Park, J.K. Song, J.S. Ha, S.M. Park, Appl. Surf. Sci. **258**, 8542 (2012)
15. H. Benzarouk, A. Drici, M. Mekhnache, A. Amara, M. Guerioune, J.C. Bernède, H. Bendjffal, Superlattices Microstruct. **52**, 594 (2012)
16. S. Aksoy, Y. Caglar, S. Ilican, M. Caglar, J. Alloys Compd. **512**, 171 (2012)
17. D. Fang, P. Yao, H. Li, Ceram. Int. **40**, 5873 (2014)
18. G. Vijayaprasath, G. Ravi, M.R. Manikandan, M. Arivananhan, M. Navaneethan, Y. Hayakawa, Asian J. Chem. **25**, S258 (2013)
19. R. Chandramohan, J. Thirumalai, T.A. Vijayan, S. Valanarasu, S.E. Vizhian, M. Srikanth, V. Swaminathan, Adv. Sci. Lett. **3**, 319 (2010)
20. J. Tang, J. Chai, J. Huang, L. Deng, X.S. Nguyen, L. Sun, T. Venkatesan, Z. Shen, C.B. Tay, S.J. Chua, A.C.S. Appl, Mater. Interfaces **7**, 4737 (2015)
21. I. Polat, S. Yılmaz, E. Bacaksız, Y. Atasoy, M. Tomakin, J. Mater. Sci:Mater. Electron. **25**, 3173 (2014)
22. L. Roza, K.A.J. Fairuzy, P. Dewanta, A.A. Umar, M.Y.A. Rahman, M.M. Salleh, J. Mater. Sci.: Mater. Electron. **26**, 7955 (2015)
23. Z. Wang, M. Wang, Z. Lin, Y. Xue, G. Huang, X. Yao, Appl. Surf. Sci. **255**, 4705 (2009)
24. S. Singh, G.R. Dillip, S. Vyas, M. Roqibul Hasan, I.-K. Park, P. Chakrabarti, S.-H. Park, Microsyst. Technol. (2015). doi:10.1007/s00542-015-2724-z
25. W.-C. Huang, T.-C. Lin, T.-L. Hsien, M.-H. Tsai, C.-T. Horng, T.-L. Kuo, Microelectron. Eng. **107**, 205 (2013)
26. M. Soylu, O. Savas, Mater. Sci. Semicond. Process. **29**, 76 (2015)
27. T. Tsuboi, K. Yamamoto, A. Nakamura, J. Temmyo, Jpn. J. Appl. Phys. **49**, 04DG13 (2010)
28. S. Ilican, F. Yakuphanoglu, M. Caglar, Y. Caglar, J. Alloys Compd. **509**, 5290 (2011)
29. C.S. Barret, T.B. Massalski, *Structure of Metals*, 3rd edn. (Pergamon Press, Oxford, 1980)
30. P. Kubelka, F. Munk, Z. Tech. Physik. **12**, 593 (1931)
31. H. Peng, P.F. Ndione, D.S. Ginley, A. Zakutayev, S. Lany, Phys. Rev. X **5**, 1 (2015)
32. A.A. Ahmad, A.M. Alsaad, B.A. Albiss, M.-A. Al-Akhras, H.M. El-Nasser, I.A. Qattan, Thin Solid Films **606**, 133 (2016)
33. C. Mao, L. Fang, H. Zhang, W. Li, F. Wu, G. Qin, H. Ruan, C. Kong, J. Alloys Compd. **676**, 135 (2016)
34. K. Joshi, M. Rawat, S.K. Gautam, R.G. Singh, R.C. Ramola, F. Singh, J. Alloys Compd. **680**, 252 (2016)
35. S. Akir, A. Barras, Y. Coffinier, M. Bououdina, R. Boukherroub, A.D. Omrani, Ceram. Int. **42**, 10259 (2016)
36. S. Klubnuan, P. Amornpitoksuk, S. Suwanboon, Mater. Sci. Semicond. Process. **39**, 515 (2015)
37. S. Suwanboon, P. Amornpitoksuk, A. Sukolrat, Ceram. Int. **37**, 1359 (2011)
38. S.M. Sze, *Physics of Semiconductor Devices*, 2nd edn. (Wiley, New York, 2002)
39. S. Sharma, C. Periasamy, Superlattices Microstruct. **73**, 12 (2014)
40. F.Z. Bedia, A. Bedia, B. Benyoucef, S. Hamzaoui, Phys. Proc. **55**, 61 (2014)
41. P. Klason, M.M. Rahman, Q.H. Hu, O. Nur, R. Turan, M. Willander, Microelectron. J. **40**, 706 (2009)
42. N. Zebbar, Y. Kheireddine, K. Mokeddem, A. Hafdallah, M. Kechouane, M.S. Aida, Mater. Sci. Semicond. Process. **14**, 229 (2011)
43. S. Aydoğan, K. Çınar, H. Asıl, C. Coşkun, A. Türüt, J. Alloys Compd. **476**, 913 (2009)
44. G.B. Sakr, S.S. Fouad, I.S. Yahia, D.M.A. Basset, F. Yakuphanoglu, Mater. Res. Bull. **48**, 752 (2013)
45. M.A. Lampert, P. Mark, *Current Injection in Solids* (Academic Press, NY, 1970)
46. S. Aksoy, Y. Caglar, J. Alloys Compd. **613**, 330 (2014)
47. S.K. Cheung, N.W. Cheung, Appl. Phys. Lett. **49**, 85 (1986)
48. R.K. Gupta, K. Ghosh, P.K. Kahol, Physica. E. **41**, 617 (2009)
49. H. Norde, J. Appl. Phys. **50**, 5052 (1979)
50. R.K. Gupta, F. Yakuphanoglu, K. Ghosh, P.K. Kahol, Microelectron. Eng. **88**, 3067 (2001)
51. A. Van der Ziel, *Solid State Physical Electronics*, 2nd edn. (Prentice-Hall, Englewood Cliffs, 1968)